

# Diversity of flux avalanche patterns in superconducting films

J. I. Vestgård,<sup>1</sup> D. V. Shantsev,<sup>1</sup> Y. M. Galperin,<sup>1,2</sup> and T. H. Johansen<sup>1,3</sup>

<sup>1</sup>*Department of Physics, University of Oslo, P. O. Box 1048 Blindern, 0316 Oslo, Norway*

<sup>2</sup>*Physico-Technical Institute RAS, 194021 St. Petersburg, Russian Federation*

<sup>3</sup>*Institute for Superconducting and Electronic Materials,  
University of Wollongong, Northfields Avenue, Wollongong, NSW 2522, Australia*

The variety of morphologies in flux patterns created by thermomagnetic dendritic avalanches in type-II superconducting films is investigated using numerical simulations. The avalanches are triggered by introducing a hot spot at the edge of a strip-shaped sample, which is initially prepared in a partially penetrated Bean critical state by slowly ramping the transversely applied magnetic field. The simulation scheme is based on a model accounting for the nonlinear and nonlocal electrodynamics of superconductors in the transverse geometry. By systematically varying the parameters representing the Joule heating, heat conduction in the film, and heat transfer to the substrate, a wide variety of avalanche patterns is formed, and quantitative characterization of areal extension, branch width etc. is made. The results show that branching is suppressed by the lateral heat diffusion, while large Joule heating gives many branches, and heat removal into the substrate limits the areal size. The morphology shows significant dependence also on the initial flux penetration depth.

PACS numbers: 74.25.Ha, 68.60.Dv, 74.78.-w

## I. INTRODUCTION

The gradual flux penetration in type-II superconducting films is occasionally interrupted when large amounts of magnetic flux rush in from the edges, forming complex dendritic patterns inside the specimen. Experiments using magneto-optical imaging have revealed that such dendritic avalanches take place in numerous materials, e.g., Nb,<sup>1</sup> YBa<sub>2</sub>Cu<sub>3</sub>O<sub>7-x</sub>,<sup>2-4</sup> MgB<sub>2</sub>,<sup>5,6</sup> Nb<sub>3</sub>Sn,<sup>7</sup> YNi<sub>2</sub>B<sub>2</sub>C,<sup>8</sup> Pb<sup>9</sup> and NbN;<sup>10</sup> see also Ref. 11 for a review. The similarity in the avalanche morphology in so different materials strongly suggests that the origin of the phenomenon is of a universal nature. Indeed, it is today widely agreed that the dendritic instability originates from a thermomagnetic breakdown in the superconductor.<sup>12</sup> This can occur when a small temperature fluctuation locally weakens the pinning of the vortices, causing some magnetic flux to advance into the superconductor. Since moving flux releases heat, the local temperature then increases further, and a positive feedback loop is formed, which can lead to a rapid runaway in the temperature and magnetic flux propagation.

In superconducting films placed in perpendicular magnetic fields, the nonlocal electrodynamics complicates the theoretical description of the instability. Thus, an analytical treatment was largely delayed compared to the bulk case, and in particular, the conditions for instability onset, and the origin of a fingering nature of the avalanches in the film case were explained only relatively recently.<sup>13-15</sup> To follow the complete time evolution of dendritic avalanches, including the cascades of branching events, only numerical simulations have proved successful and indeed produced very realistic results.<sup>15-17</sup> However, so far little work has been done to systematically characterize these patterns, and to our knowledge, no effort was made trying to identify how various physical parameters influence the morphology of the avalanches.

Such characterization is not readily done experimentally since in practice it is difficult to vary the material parameters independently. Hence, the most feasible way to make a systematic investigation is to carry out a numerical simulation study. In this paper we present results of such a systematic study of the morphology of dendritic flux patterns resulting from the thermomagnetic instability in superconducting films. First, we identify the dimensionless parameters that enter the governing equations. Then, avalanches are nucleated at an edge, where partially penetrated critical-states serve as initial conditions, and we follow the avalanche evolution until it ends in a frozen flux pattern. The final patterns created using different parameter values are compared, analyzed quantitatively and discussed.

The paper is organized as follows: Section II describes the model and introduces the key dimensionless parameters. Section III reports and discusses the results of our simulations where those parameters are systematically varied. In addition, the dependence of the avalanche patterns on the initial critical-state is investigated. The results are summarized in Sec. IV.

## II. MODEL

Consider a long superconducting strip of half-width  $w$  and thickness  $d \ll w$ , in thermal contact with a substrate, see Fig. 1. In the numerical simulations the following strategy is used: Starting from a zero-field-cooled strip, we slowly ramp (increase) the applied magnetic field  $H_a$ , while the thermal feedback is turned off. This ensures that the flux penetration is gradual and the temperature is everywhere equal to the substrate temperature  $T_0$ . The spatial distributions of flux density  $B_z$  and sheet current  $\mathbf{J}$  develop in agreement with the critical state model for the transverse geometry.<sup>18</sup> The field

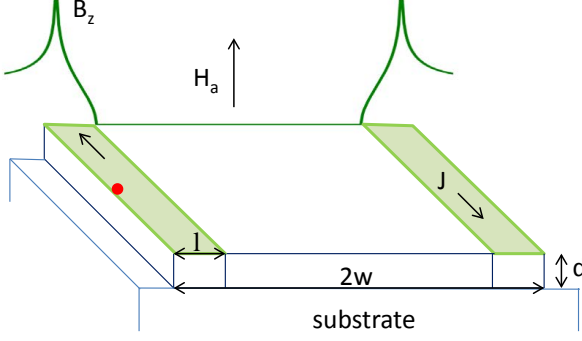


FIG. 1. Sketch of the sample configuration. A long superconducting strip of thickness  $d$  and half-width  $w$ , is in thermal contact with a substrate. Over a region of width  $l$  near both edges a critical state with sheet current  $J = J_c$  and flux density  $B_z$  exists as a hot-spot (red dot) is introduced to trigger an avalanche.

ramp is stopped when the flux penetration reaches the depth,  $l$ , where  $l/w \sim 0.1$ , and that state is taken as initial condition for the upcoming avalanche. The thermal feedback is then turned on, and a heat pulse is applied to a small region near the edge, thus triggering the instability. The same protocol is repeated using different sample parameters, and for each run we analyze the size and morphology of the flux distribution frozen in the superconductor after the avalanche.

Before describing the physical model in detail, let us introduce the units that will be used. Time is expressed in units of  $t_0 = \mu_0 dw / \rho_n$ , where  $\mu_0$  is the vacuum magnetic permeability and  $\rho_n$  is the normal-state resistivity of the superconductor. The sheet current  $\mathbf{J}$  and magnetic field  $B_z / \mu_0$  are both expressed in units of the zero-temperature critical sheet current,  $J_{c0} = dj_{c0}$ . The temperature  $T$  is normalized to the critical value  $T_c$ , and the spatial coordinates  $(x, y)$  are in units of  $w$ . Consequently, the Faraday law,  $\dot{\mathbf{B}} = -\nabla \times \mathbf{E}$ , implies that the electric field  $\mathbf{E}$  is normalized by  $\rho_n j_{c0}$ .

We consider a superconductor described by a non-retarded relationship between the electrical field and the current density as follows:<sup>19</sup>

$$\mathbf{E} = \rho \mathbf{J}, \quad \rho = \begin{cases} 1, & \text{if } J > J_c \text{ or } T > 1, \\ (J/J_c)^{n-1}, & \text{otherwise.} \end{cases} \quad (1)$$

Here  $J \equiv |\mathbf{J}|$  while  $n$  is the creep exponent. The temperature dependencies of  $n$  and  $J_c$  are taken as<sup>6,16</sup>

$$\begin{aligned} J_c(T) &= 1 - T, \\ n(T) &= n_1/T + n_0. \end{aligned} \quad (2)$$

The thermal properties of the superconducting film are specified by the temperature dependence of the specific heat  $c$ , thermal conductivity  $\kappa$ , and the coefficient of heat removal to the substrate  $h$ . We use here an approximation applied successfully in previous modelling

work, namely that all three parameters have cubic  $T$ -dependencies.<sup>20</sup>

Based on this, the evolution of the local temperature is described by the dimensionless diffusion equation,

$$\dot{T} = \alpha \nabla^2 T - \beta(T - T_0) + \gamma T^{-3} \mathbf{J} \cdot \mathbf{E}, \quad (3)$$

where  $T_0$  is the normalized substrate temperature. The coefficients

$$\alpha = \frac{d}{w} \frac{\mu_0 \kappa}{\rho_n c}, \quad \beta = w \frac{\mu_0 h}{\rho_n c}, \quad \gamma = wd \frac{\mu_0 j_{c0}^2}{c T_c}, \quad (4)$$

are also dimensionless, and involve  $c$ ,  $\kappa$  and  $h$  evaluated at  $T_c$ . The parameter  $\alpha$  has the meaning of a normalized coefficient of thermal diffusion, and characterizes the smearing of  $T$  due to heat conduction within the film. The  $\beta$  characterizes the heat flow to the substrate, while  $\gamma$  measures the positive feedback due to Joule heating. For  $\gamma = 0$  the evolution of the magnetic flux and temperature distributions are decoupled and the film is always thermomagnetically stable.

Note that in this representation the parameter space is significantly reduced compared to the dimensional description, since all the  $\kappa, h, c, T_c, j_{c0}$ , and  $\rho_n$  have been combined into three dimensionless parameters.

To calculate the electromagnetic behavior we express the sheet current through the local magnetization,  $g$ , as

$$J_x = \partial g / \partial y, \quad J_y = -\partial g / \partial x. \quad (5)$$

Outside the sample,  $g$  vanishes by definition. In an infinite or periodic space, the Biot-Savart law for a thin film has a simple expression in the Fourier space. Inverting it and taking the time derivative yields<sup>16</sup>

$$\dot{g} = \mathcal{F}^{-1} \left[ \frac{2}{k} \mathcal{F} \left( \frac{\dot{B}_z}{\mu_0} - \dot{H}_a \right) \right], \quad (6)$$

where  $\mathcal{F}$  and  $\mathcal{F}^{-1}$  are the forward and inverse Fourier transform, respectively, and  $k = \sqrt{k_x^2 + k_y^2}$  is the in-plane wave-vector. Inside the sample, the right-hand side of Eq. (6) is found from the Faraday law in combination with the material law, Eq. (1). Outside,  $\dot{B}_z$  is found implicitly by an iterative scheme requiring that  $\dot{g} = 0$ . More details about the simulation procedure are found in Ref. 16.

The sample occupies a  $2 \times 2$  square, with periodic boundary conditions in one direction. The other direction is extended with extra space in order to take into account the magnetic field outside the strip. The total area of the simulation covers a rectangle of size  $3 \times 2$ , which is discretized on a  $768 \times 512$  equidistant grid.

The simulations were carried out using  $T_0 = 0.15$ , and the creep exponent was set to  $n = 20/T - 10$ . The initial state was prepared with a ramp rate of  $\dot{H}_a = 10^{-5}$ , and the hot spot triggering the avalanche had a size of  $0.01 \times 0.01$  (a cross consisting of 5 grid points) and a temperature of  $T = 1.5$ . During the avalanche the field ramp was stopped.

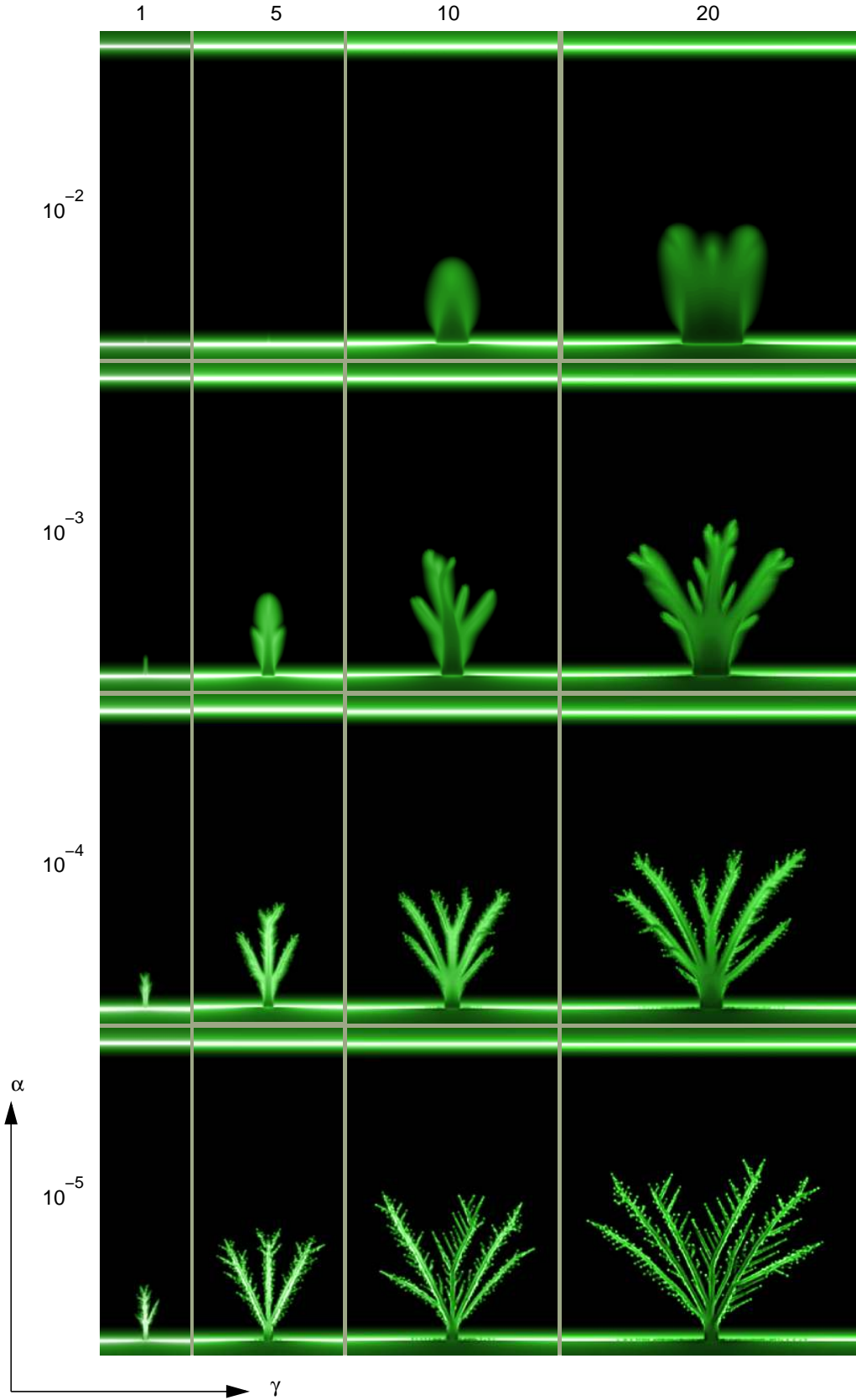


FIG. 2. Variety of avalanche flux distributions  $B_z$  arranged in a matrix of panels with constant  $\alpha$  in the rows, and with constant  $\gamma$  in the columns. The image brightness represents the magnitude of  $B_z$ , as in experimental magneto-optical images, and the strip edges are seen as a pair of bright horizontal lines while the dark area between them is the flux-free Meissner state region of the superconducting strip.

### III. RESULTS AND DISCUSSION

The parameter space in these simulations is three-dimensional, and we present and discuss first the various types of flux patterns produced with  $\beta = 0.1$ , i.e., keeping a fixed coefficient of heat transfer to the substrate. The initial flux penetration depth was  $l = 0.11$  when a hot spot was introduced to trigger an avalanche.

#### A. Varying $\alpha$ and $\gamma$

Figure 2 displays a collection of final-state flux avalanche patterns obtained using values for  $\alpha$  and  $\gamma$  in the range  $10^{-5} - 10^{-2}$  and  $1 - 20$ , respectively. Evidently, within this part of parameter space one finds patterns which show striking similarities with those observed in experiments.<sup>1-9</sup> In addition, we find some type of patterns not previously reported.

The figure shows that with an increasing Joule heating,  $\gamma$ , and a constant  $\alpha$ , the avalanches quickly become larger in size and get more and more branches. At the same time, the branch width remains essentially the same, although for increasing  $\gamma$  the main trunk near the edge gets steadily wider.

When instead keeping  $\gamma$  constant and increasing the in-plane heat diffusion,  $\alpha$ , one sees that the number of branches decreases significantly. At the same time, the overall avalanche size is not varying much. At maximum value,  $\alpha = 10^{-2}$ , the avalanches can hardly be characterized as dendritic, but rather as a soft protrusion. Such non-dendritic shapes is a consequence of the thermal diffusion being almost as fast as the electromagnetic propagation.

The simulated  $B_z$ -maps reveal also several other interesting features. One is that one never finds branching to take place inside the critical-state region near the edge. Another is that even in the largest avalanches, the branches rarely propagate past the sample center. Furthermore, branches never overlap, thus appearing to repel each other. Yet another is that the inner part of the branches most often has the highest flux density, but in some cases they show a dark low- $B_z$  core. Note also that the flux density is always reduced in the avalanche trunk as well as outside the sample, next to the root location. All these features correspond very well with experimental observations using magneto-optical imaging, thus demonstrating a detailed correspondence between our simulations and reality.

A feature seen in Fig. 2 which so far was not reported neither from experiments nor from previous simulations, is the appearance of quasi-periodic side branches in the panels with small  $\alpha$ . The origin of these branches is not yet clear, but a similar phenomenon is known from other systems, e.g., formation of dendrites in crystal growth.<sup>21</sup>

The panels in the upper left corner of Fig. 2, corresponding to small  $\gamma$  and large  $\alpha$ , do not show any visible trace of avalanche activity. This indicates the existence

of a region in parameter space where the system is stable towards even large perturbations, such as local heating above  $T_c$ . Hence, a guiding line for design of, e.g., superconducting power-devices is to make materials and dimensions such that  $\gamma$  is small and  $\alpha$  is large. Note that the transition between stable and unstable behavior is a crossover rather than a sharp phase boundary.

Finally, note also that the flux structures in Fig. 2 are more symmetric and with straighter branches than the avalanche structures reported from previous simulation work using the same formalism.<sup>16,17</sup> This difference is due to the fact that in previous work static disorder was introduced in the critical current density whereas here the sample was perfectly uniform. Regarding the role of disorder we therefore conclude that (i) Branching flux patterns may appear even in uniform materials, in agreement with theoretical predictions of the fingering instability in a uniform system.<sup>13-15</sup> (ii) It is the non-linear and nonlocal electrodynamics, rather than spatial disorder, that is responsible for the branching of the flux structures. (iii) The presence of disorder affects the exact path along which the hot branches propagate. Straight main branches with quasi-periodic side branches in a uniform sample become wiggly and lose periodicity in a disordered sample. (iv) Figure 2 shows no sign of symmetric bifurcations, suggesting that the process of symmetric tip splitting found in Ref. 17 is also driven by disorder.

As a quantitative measure of the effect of varying  $\gamma$  and  $\alpha$ , Fig. 3 shows the total avalanche size, taken as the area of the Meissner state region invaded by flux, plotted as a function of  $\gamma$  for various  $\alpha$ . In spite that  $\alpha$  spans 4 decades the graphs are not very different and increase almost linearly with the same slope. Evidently, the Joule heating parameter  $\gamma$  is a crucially important

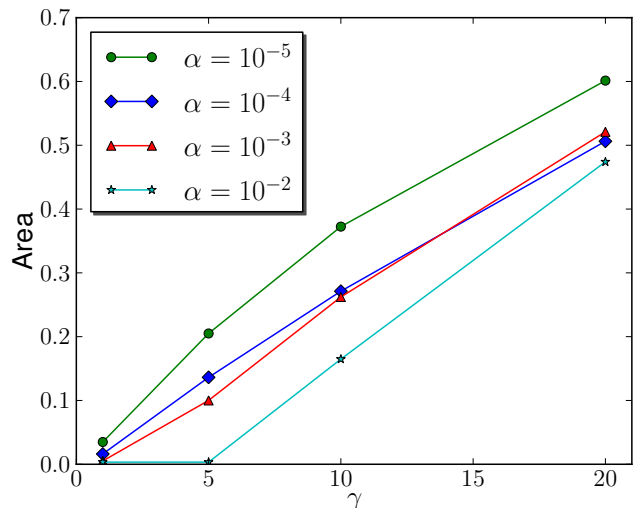


FIG. 3. Avalanche size in units of  $w^2$  as a function of  $\gamma$  for different  $\alpha$ . The data are extracted from the flux patterns displayed in the panels of Fig. 2.

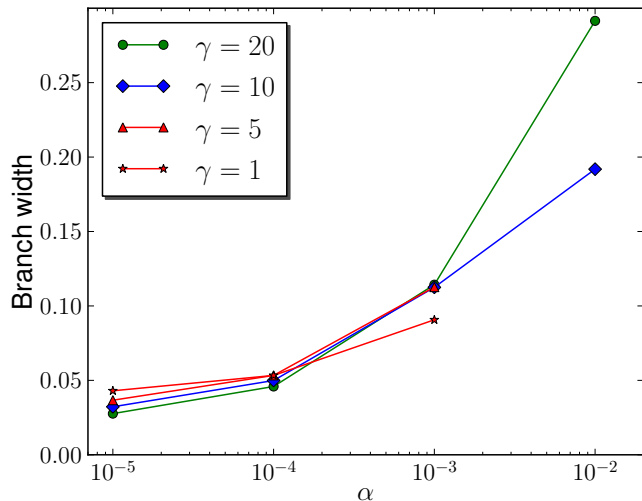


FIG. 4. Average branch width in units of  $w$  as function of  $\alpha$  for various  $\gamma$ , extracted from the flux patterns shown in Fig. 2.

for the impact of an avalanche.

Presented in Fig. 4 is the average branch width plotted as a function of  $\alpha$  for various  $\gamma$ . The width is evaluated by dividing the area of the avalanche by the length of the contour of  $B_z = 0$  around the structure. The figure shows that the width grows rapidly with increasing  $\alpha$ , and is quite weakly depending on  $\gamma$ . This suggests

that the width of the individual branches in the dendritic structure to a large extent is controlled by thermal diffusion.

### B. Varying $\beta$

Consider next how the avalanche morphology is influenced by varying the heat transfer to the substrate characterized by the parameter  $\beta$ . Figure 5 illustrates the variety of flux patterns obtained for  $\beta$  ranging from 0.1 to 100, while keeping constant the parameters  $\alpha = 10^{-4}$ ,  $\gamma = 10$ , and  $l = 0.11$ . It is evident that an increase in  $\beta$  leads to avalanches of smaller overall size and thinner branches, and to some extent, also less degree of branching. The behavior can be understood from the role of  $\beta$  in the heat diffusion equation, Eq. (3). During an avalanche the term proportional to  $\beta$  represents a heat-sink that stabilizes the runaway and thus tend to terminate the avalanche.<sup>17</sup> A large heat sink effect is also expected to give thinner branches.

### C. Varying $l$

Finally, we consider how the avalanches depend on the penetration depth,  $l$ , of the critical-state background flux distribution. Shown in Fig. 6 are four images of the strip where  $l$  varies from 0.04 to 0.3 while  $\alpha$ ,  $\beta$  and  $\gamma$  are kept constant. One sees that large  $l$  also gives large avalanches

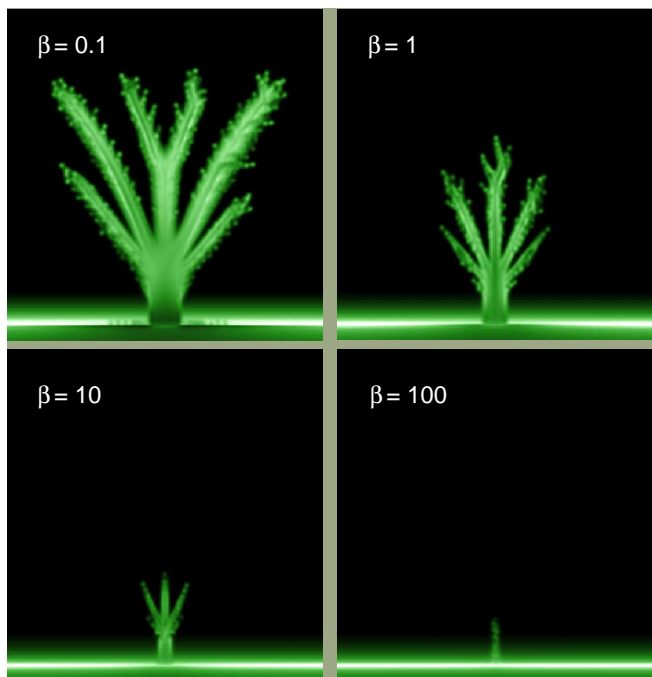


FIG. 5. Avalanche flux patterns  $B_z$  obtained for various  $\beta$ , keeping constant  $\alpha = 10^{-4}$ ,  $\gamma = 10$  and  $l = 0.11$ . These panels show only the lower half of the strip.

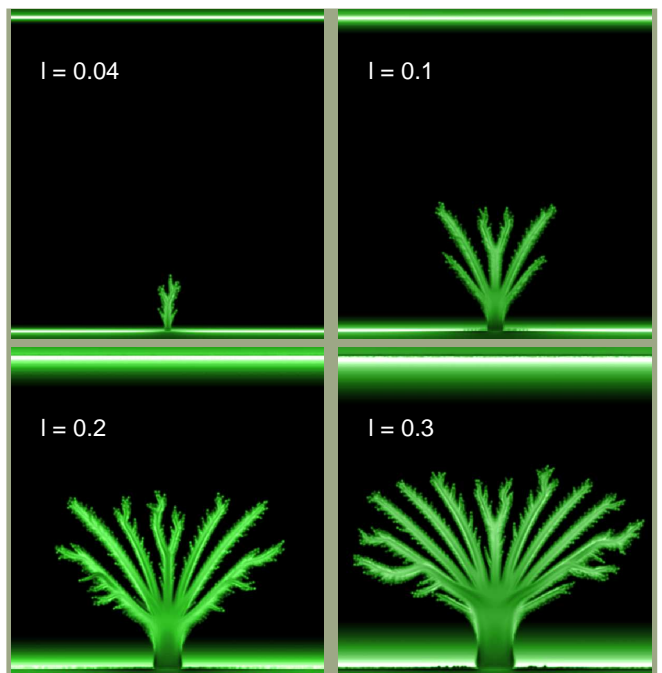


FIG. 6. Flux distributions  $B_z$  for avalanches nucleated at different critical-state penetration depths  $l = 0.04, 0.1, 0.2$ , and  $0.3$ , with  $\alpha = 10^{-4}$ ,  $\beta = 0.1$  and  $\gamma = 10$ .

and many branches. This results is in agreement with previous experiment by Bolz et al.<sup>4</sup>

The images seen in Fig. 6 show also a striking resemblance with previous experimental and simulation results at different substrate temperatures  $T_0$ .<sup>5,16</sup> The results of this work suggests that the increasing avalanche size with  $T_0$  is not because the avalanche propagation is sensitive to  $T_0$ , but rather because it is sensitive to the flux penetration depth prior to the avalanches, which increases with  $T_0$ .

#### IV. SUMMARY

In this work we have used numerical simulations to investigate how the dimensionless material parameters affect the size and morphologies of dendritic flux avalanches in superconducting films. The avalanches were nucleated at the edge of a strip by a heat pulse and by varying the parameters we have reproduced a wide range of morphologies previously seen experimentally. We find that increasing the normalized coefficient of heat diffusion  $\alpha$  gives fewer and wider branches while strong heat removal

to the substrate, quantified by  $\beta$ , cause smaller total avalanche size and thinner branches. Increasing values for the Joule heating parameter  $\gamma$  gives more branches and larger avalanches. Parameter combinations with large  $\alpha$  and small  $\gamma$  proved to be stable towards large perturbations. Quasi-periodic side branches were seen in the dendritic structures with small  $\alpha$ , and their existence was attributed to the absence of spatial disorder. Finally, we found that the avalanche morphology is sensitive to the initial critical state before the avalanche, namely, deeper initial penetration gives larger and more branching avalanches.

For future work, it will be of interest to use the present dimensionless description to study how the linear stability diagram of superconductors is affected by varying the parameters  $\alpha$ ,  $\beta$ , and  $\gamma$ .

#### ACKNOWLEDGMENTS

The financial support from the Research Council of Norway is greatly acknowledged.

- 
- <sup>1</sup> C. A. Durán, P. L. Gammel, R. E. Miller, and D. J. Bishop, *Phys. Rev. B* **52**, 75 (1995).
  - <sup>2</sup> P. Brüll, D. Kirchgässner, P. Leiderer, P. Berberich, and H. Kinder, *Ann. Phys. (Leipzig)* **1**, 243 (1992).
  - <sup>3</sup> P. Leiderer, J. Boneberg, P. Brüll, V. Bujok, and S. Herminghaus, *Phys. Rev. Lett.* **71**, 2646 (1993).
  - <sup>4</sup> U. Bolz, J. Eisenmenger, J. Schiessling, B.-U. Runge, and P. Leiderer, *Physica B* **284**, 757 (2000).
  - <sup>5</sup> T. H. Johansen, M. Baziljevich, D. V. Shantsev, P. E. Goa, Y. M. Galperin, W. N. Kang, H. J. Kim, E. M. Choi, M.-S. Kim, and I. Lee, *Europhys. Lett.* **59**, 599 (2002).
  - <sup>6</sup> Z. X. Ye, Q. Li, Y. F. Hu, A. V. Pogrebnyakov, Y. Cui, X. X. Xi, J. M. Redwing, and Q. Li, *Appl. Phys. Lett.* **85**, 5284 (2004).
  - <sup>7</sup> I. A. Rudnev, S. V. Antonenko, D. V. Shantsev, T. H. Johansen, and A. E. Primenko, *Cryogenics* **43** (2003).
  - <sup>8</sup> S. C. Wimbush, B. Holzapfel, and Ch. Jooss, *J. App. Phys.* **96**, 3589 (2004).
  - <sup>9</sup> V. Vlasko-Vlasov, U. Welp, V. Metlushko, and G. W. Crabtree, *Physica C* **341**, 1281 (2000).
  - <sup>10</sup> I. A. Rudnev, D. V. Shantsev, T. H. Johansen, and A. E. Primenko, *Appl. Phys. Lett.* **87**, 04202 (2005).
  - <sup>11</sup> E. Altshuler and T. H. Johansen, *Rev. Mod. Phys.* **76**, 471 (2004).
  - <sup>12</sup> R. G. Mints and A. L. Rakhmanov, *Rev. Mod. Phys.* **53**, 551 (1981).
  - <sup>13</sup> A. L. Rakhmanov, D. V. Shantsev, Y. M. Galperin, and T. H. Johansen, *Phys. Rev. B* **70**, 224502 (2004).
  - <sup>14</sup> D. V. Denisov, A. L. Rakhmanov, D. V. Shantsev, Y. M. Galperin, and T. H. Johansen, *Phys. Rev. B* **73**, 014512 (2006).
  - <sup>15</sup> I. S. Aranson, A. Gurevich, M. S. Welling, R. J. Wijngaarden, V. K. Vlasko-Vlasov, V. M. Vinokur, and U. Welp, *Phys. Rev. Lett.* **94**, 037002 (2005).
  - <sup>16</sup> J. I. Vestgård, D. V. Shantsev, Y. M. Galperin, and T. H. Johansen, *Phys. Rev. B* **84**, 054537 (2011).
  - <sup>17</sup> J. I. Vestgård, D. V. Shantsev, Y. M. Galperin, and T. H. Johansen, *Sci. Rep.* **2**, 886 (2012).
  - <sup>18</sup> E. H. Brandt and M. Indenbom, *Phys. Rev. B* **48**, 12893 (1993).
  - <sup>19</sup> E. H. Brandt, *Phys. Rev. B* **52**, 15442 (1995).
  - <sup>20</sup> D. V. Denisov, D. V. Shantsev, Y. M. Galperin, E.-M. Choi, H.-S. Lee, S.-I. Lee, A. V. Bobyl, P. E. Goa, A. A. F. Olsen, and T. H. Johansen, *Phys. Rev. Lett.* **97**, 077002 (2006).
  - <sup>21</sup> J. S. Langer, *Rev. Mod. Phys.* **52**, 1 (1980).